Dear Mr. Thomsen,

I am pleased to inform you that your revised manuscript, referenced below, has been accepted for publication in Medical Physics in the following section: Research Article.

"A new algorithm for estimating the rod volume fraction and the trabecular thickness from in vivo computed tomography"

Once your manuscript has been received by AIP Production Services, you will receive an email with your assigned AIP ID number. When your page proofs are ready for your review, you will receive another e-mail from AIP Production Services. If your manuscript includes a URL, you must verify that the URL is accessible at the time that you review the page proofs. Direct all questions pertaining to papers in the production process to the contact information supplied in that e-mail. Be sure to include the AIP Production Number on all correspondence.

During the production process, authors may access information about their accepted manuscript, including projected publication date, by visiting the AMSIS website at:

http://authorportal.aip.org/amsis/status.html

To use this service, you must supply the last name of one of the first three authors and either an Editor Code or AIP ID number. The Editor Code is your manuscript tracking number: 16-854R. The AIP ID number will be provided to you by AIP Production Services when they receive your manuscript.

ATTENTION: Authors of NIH-funded papers

In compliance with the National Institutes of Health (NIH) Public Access Policy, the AAPM has authorized the American Institute of Physics (AIP) to deposit your Medical Physics article in Pub Med Central.

In 1-3 weeks after your article has been published online, it will be automatically deposited in final, published form, along with its associated metadata. AIP will provide you with the PMC ID number via email, once it has been assigned. Please note that the full text of the article will not become available on PMC until after a one-year embargo. No action is required on your part, but we do ask that you please inform your co-authors of the procedure.

Please check that you have properly credited the NIH in the Acknowledgment section of your paper.

For information pertaining to the NIH policy, please visit:
http://www.pubmedcentral.nih.gov/about/pubinfo.html

Thank you for your contribution to the Journal. If you have any questions, feel free to contact us at journal@aapm.org.

Sincerely,

Shiva K. Das, Ph.D., Therapy Physics Editor
Jeffrey F. Williamson, Ph.D., Editor-in-Chief
Medical Physics
AAPM
1631 Prince Street, Alexandria, VA 22314

Editor's Comments:
Thank you.

Reviewer Comments:
Associate Editor and Reviewer comments are attached to this email.

MEDPHYS_email_attachment_DEC_LTR_reviewer_summary_96752_1_1477541534.html

Referee #1's Comments

Note	Comment
Novelty of manuscript in its current form (Comment)	Showed that the application of a fractal method improved the prediction of failure load as compared to standard micro-structural parameters.

Referee #2's Comments

Note	Comment
Free Form Review	This paper has been revised based on reviewer's comments. Authors answered reviewers' questions and improved manuscript. I don't have any other comments.

Associate Editor's Comments

Note	Comment
Associate Editor Comments to Author	The paper is substantially improved.

Editor's Comments

Note	Comment
Remarks to Author	Thank you.

70

A new algorithm for estimating the rod volume fraction and the trabecular thickness from *in vivo* computed tomography

Felix Sebastian Leo Thomsen[1], Jaime Andrés Peña[2], Yongtao Lu[3,4], Gerd Huber[4,] Michael Morlock[4], Claus-Christian Glüer[2], Claudio Augusto Delrieux[1]

[1]National Scientific and Technical Research Council (CONICET), National University of the South, Bahía Blanca, Argentina. [2]Section Biomedical Imaging, Department of Radiology and Neurology, University Hospital Schleswig-Holstein, Campus Kiel, Germany. [3]Department of Engineering Mechanics, Dalian University of Technology, Dalian, China. [4]Institute of Biomechanics, Hamburg University of Technology, Hamburg, Germany.

Address for correspondence: Felix Thomsen, Avenida Alem 1253, 8000-Bahía Blanca, Argentina, Felix.Thomsen@uns.edu.ar

Abstract

Purpose: Existing micro-structure parameters are able to predict vertebral *in vitro* failure load, but for noisy *in vivo* data more complex algorithms are needed for a robust assessment.

Methods: A new algorithm is proposed for the micro-structural analysis of trabecular bone under *in vivo* quantitative computed tomography (QCT). Five fractal parameters are computed: (1) the average local fractal dimension FD, (2) its standard deviation FD.SD, (3) the fractal rod volume ratio fRV/BV, (4) the average fractal trabecular thickness fTb.Th and (5) its coefficient of variation fTb.Th.CV. The algorithm requires neither an explicit skeletonization of the trabecular bone, nor a well-defined transition between bone and marrow phase. Two experiments were conducted to compare the fractal with established micro-structural parameters. In the first, 20 volumes-of-interest of embedded vertebrae phantoms were scanned five times under QCT and high-resolution (HR-)QCT and once under peripheral HRQCT (HRpQCT), to derive accuracy and precision. In the second experiment, correlations between *in vitro* HRQCT structural parameters were obtained from 76 human T_{11}, T_{12} or L_1 vertebrae. *In vitro* fracture data were available for a subset of 17 human T_{12} vertebrae so that linear regression models between failure load and micro-structural HRQCT parameters could be analyzed.

Results: The results showed correlations of fTb.Th and fRV/BV with their non-fractal pendants trabecular thickness (Tb.Th) and respective structure model index (SMI) while higher precision and accuracy was observed on the fractal measures. Linear models of bone mineral density with two and three fractal micro-structural HRQCT parameters explained 86% and 90% (adjusted R^2) of the failure load and significantly improved the linear models based only on BMD and established standard micro-structural parameters (68% - 77% adjusted R^2).

Conclusion: The application of fractal methods may grant further insight in the study of bone quality *in vivo* when image resolution and quality are less than optimal for current standard methods.

Keywords: local fractal dimension, rod volume ratio, trabecular thickness, failure load, QCT

Introduction

Quantitative computed tomography (QCT) is a clinical *in vivo* 3D image modality that allows visualization and quantitative assessment of the spongy microstructure of human vertebrae. In particular, QCT can be used for diagnosis and monitoring of osteoporosis. Bone quality encompasses bone mineral density (BMD), micro architecture, turnover rates, damage accumulation, and mineralization[1]. While the extraction of BMD from QCT or even dual energy absorptiometry (DXA) is straightforward, the estimation of micro-structure parameters is more *challenging. BMD is able to account for up to 70% of variability of vertebral failure load, while* existing micro-structure parameters yield little additional information. Nevertheless, high computational power enables the application of more complex algorithms which are needed for a robust assessment of micro-structure parameters under noisy *in vivo* QCT.

Several refined algorithms have been proposed for dependent[2] and independent trabecular separation models[3-5]. Algorithms of the rod volume ratio (RV/BV) include scale

Abbreviations of the new fractal entities	
$FD_i(\vec{x})$	local fractal dimension obtained with method $i \in \{1,2\}$ at voxel $\vec{x}$
$fTb.Th(\vec{x})$	local fractal trabecular thickness at voxel $\vec{x}$
FD_i	average of $FD_i(\vec{x})$
FD_i.SD	standard deviation of $FD_i(\vec{x})$
fRV_i/BV	fractal rod volume / bone volume of $FD_i(\vec{x})$
fTb.Th	average of $fTb.Th(\vec{x})$
fTb.Th.CV	coefficient of variation of $fTb.Th(\vec{x})$

space methods[6], fuzzy approaches[7], concurrent assignments of rod- and plate-likeness on the same voxel[8], and methods to obtain simultaneously RV/BV and trabecular thickness (Tb.Th)[9]. However, most of these attempts require a well-defined transition between bone and marrow phases or a structure preserving 3D skeletonization[10]. This makes them more likely suited for HRpQCT, rather than HRQCT or QCT resolution realms. In 3D imaging, fractal methods contain similar properties as scale space methods. Due to limited computational power, early implementations of fractal concepts focused primarily on global parameters, for instance, box-counting dimensions[11]. Nowadays, different kinds of local fractal dimensions exist[12] and have been obtained from an initial slope in log-log scale between a local measure and the radii of the local neighborhood. In particular the trabecular bone score[13], a fractal dimension on the local variance of trabecular bone, extracts structural information from 2D projections[14]. However, trabecular bone score may not be suited to estimate bone strength[15].

The aim of this work is to introduce new structural parameters from QCT that (1) are robust against noise, (2) contain a semantic link to existing structural micro-structural parameters, and (3) contribute to assess key properties of bone health, such as estimations of bone strength. New fractal methods of RV/BV and Tb.Th are proposed, based on local fractal methods of the Hölder exponent[16,17]. They neither require an explicit skeletonization of trabecular bone, nor a well-defined transition between bone and marrow phases. Two experiments were conducted: the first, to assess robustness against noise on simulated *in vivo* HRQCT and QCT; the second, to obtain correlations between parameters from *ex situ* HRQCT; additionally experimentally derived failure load could be predicted from a subset of the *ex situ* HRQCT scans.

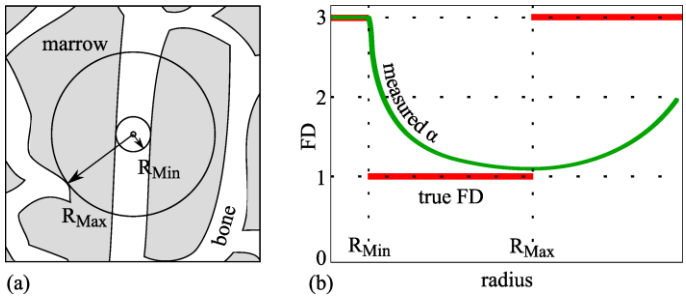

Figure 1: Evolution of α, the slope of $\log(M_r)$ vs. $\log(r)$, on a rod. α is constant 3 at $r < R_{Min}$, descends smoothly towards 1 at $r \in [R_{Min}, R_{Max}]$ and ascends again towards 3 at $r > R_{Max}$. (a) spatial illustration of M_r (b) α as a function of the radius r.

Materials and Methods

The Hölder exponent in digital images

The 3D Hölder exponent α_r relates the radius r of a sphere with the number of points (or mass) M_r inside that sphere, by computing the slope between $\log r$ and $\log M_r$:

$$\alpha_r = \lim_{a \to 1} \left(\frac{\log M_{ra} - \log M_{r/a}}{2 \log a} \right), \quad (1)$$

In the case of infinite thin points, α_r is independent of r: the Hölder exponent α is 1 on a line, 2 on a plane and 3 on a sphere. This method has been extended for digital images, where voxels are not infinite thin and to measure rods and plates instead of lines and planes. Rods and plates contain a positive trabecular thickness ($2\,R_{Min}$), causing the slope α_r to vary with r. Three different cases are met when measuring α_r on the center of a rod (Fig. 1). The slope starts at ($\alpha_r = 3$) for $r < R_{Min}$, descends smoothly towards one at $r \in [R_{Min}, R_{Max}]$ before ascending towards three at $r > R_{Max}$. The radius R_{Min} is the half of the local trabecular thickness and R_{Max} defines the maximum local radius, which does not intersect with different bone structures. The information of the local rod- or plate-likeness is hidden in the interval $r \in [R_{Min}, R_{Max}]$.

Two different methods were defined to extract the fractal dimension, the first method uses only information from the slope α_r, while the second method uses additionally information of the

curvature β_r. Firstly, when assuming that the local structure is sufficiently isolated from neighboring structures ($R_{Max} > 3R_{Min}$), the local fractal dimension $FD_1(\vec{x})$ at an arbitrary voxel $\vec{x}$ can be estimated by the minimum of α_r at $\vec{x}$:

$$FD_1(\vec{x}) = min_r\{\alpha_r(\vec{x})\}. \quad (2)$$

The estimate $FD_1(\vec{x})$ yields an overestimation of the real local fractal dimension, in particular in combination with image noise. The overestimation can be assessed by the curvature κ_r:

$$\kappa_r = \lim_{a\to 1}\tan^{-1}\left(\frac{\log M_{ra} - 2\log M_r + \log M_{r/a}}{(\log a)^2}\right). \quad (3)$$

An adjusted local slope is now estimated from a function $A(\alpha, \kappa) \in [0,3]$ which expresses the local fractal dimension in terms of slope and curvature. The local fractal dimension $FD_2(\vec{x})$ is then computed as the minimum of $A\left(\alpha_r(\vec{x}), \kappa_r(\vec{x})\right)$:

$$FD_2(\vec{x}) = min_r\left\{A\left(\alpha_r(\vec{x}), \kappa_r(\vec{x})\right)\right\}. \quad (4)$$

Since values of $\alpha_r(\vec{x})$ are generally larger than the true fractal dimension, which can be estimated with $FD_2(\vec{x})$, the ratio of $FD_2(\vec{x})/\alpha_r(\vec{x})$ grows towards one with increasing radii r. This allows to estimate the limiting radius R_{Min} from a function $\Omega(\alpha, FD_2/\alpha) \in [0,1]$, which expresses the ratio of R_{Min} and r. The local trabecular thickness $fTb.Th(\vec{x})$ is now estimated the minimum of $2r\ \Omega\left(\alpha_r(\vec{x}), FD_2/\alpha_r(\vec{x})\right)$:

$$fTb.Th(\vec{x}) = min_r\left\{2r\ \Omega\left(\alpha_r(\vec{x}), FD_2/\alpha_r(\vec{x})\right)\right\}. \quad (5)$$

The final VOI-based aggregates are computed from smoothed signals and a probability-based bone-ridge map $Ridge(\vec{x})$ (Appendix A) using the weighted average and standard deviation[18]:

$$AVG(S, Ridge) = \frac{\sum_{\vec{x}}(S \cdot Ridge)(\vec{x})}{V_1}, \quad (6)$$

$$SD(S, Ridge) = \sqrt{\frac{V_1 \sum_{\vec{x}}((S - \mu(S))^2 \cdot Ridge)(\vec{x})}{V_1^2 - V_2}}, \quad (7)$$

with $V_p = \sum_{\vec{x}} Ridge(\vec{x})^p$ and S the particular local signal. The final structural parameters for method $i \in \{1,2\}$ are the average fractal dimension:

$$\mathrm{FD_i}=AVG(FD_i, Ridge), \quad (8)$$

the standard deviation of the local fractal dimension:

$$\mathrm{FD_i.SD}=SD(FD_i, Ridge), \quad (9)$$

the fractal trabecular thickness:

$$\mathrm{fTb.Th} = AVG(fTb.Th, Ridge), \quad (10)$$

and the coefficient of variation of the local fractal trabecular thickness:

$$\mathrm{fTb.Th.CV} = \frac{SD(fTb.Th,Ridge)}{AVG(fTb.Th,Ridge)}. \quad (11)$$

The range of $FD_i(\vec{x})$ is decreased in noisy scenarios, inducing an overestimation of rods and an underestimation on plates or entirely filled regions and $FD_i(\vec{x})$ collapses to a constant value FD_i^{Noise} at a signal-to-noise ratio of 1. Under the assumption that the volume contains only rods and plates, the fractal rod volume ratio $\mathrm{fRV_i/BV}$ is defined as

$$\mathrm{fRV_i/BV} = \frac{\sum_{\vec{x}} max\left\{0, FD_i^{Noise} - FD_i(\vec{x})\right\} \cdot Ridge(\vec{x})}{\sum_{\vec{x}} \left|FD_i^{Noise} - FD_i(\vec{x})\right| \cdot Ridge(\vec{x})}, \quad (12)$$

with $FD_1^{Noise} = 2.0$ and $FD_2^{Noise} = 1.45$ at a threshold value generating BV/TV=25%. Details of the structural element, the preprocessing of the input volume, the definition of the ridge map, the smoothing procedure and the computation of $A(\alpha, \kappa)$ and $\Omega(\alpha, FD_2/\alpha)$ are provided in Appendix A. Figure 2 shows the application of a phantom of three rods and plates under noiseless and noisy conditions. The signal $FD_1(\vec{x})$ contains low variation inside rods or plates, and $FD_2(\vec{x})$ minimizes the error with the ground-truth. The algorithm was developed in MATLAB (v8.1, The MathWorks Inc., Natick, MA, USA).

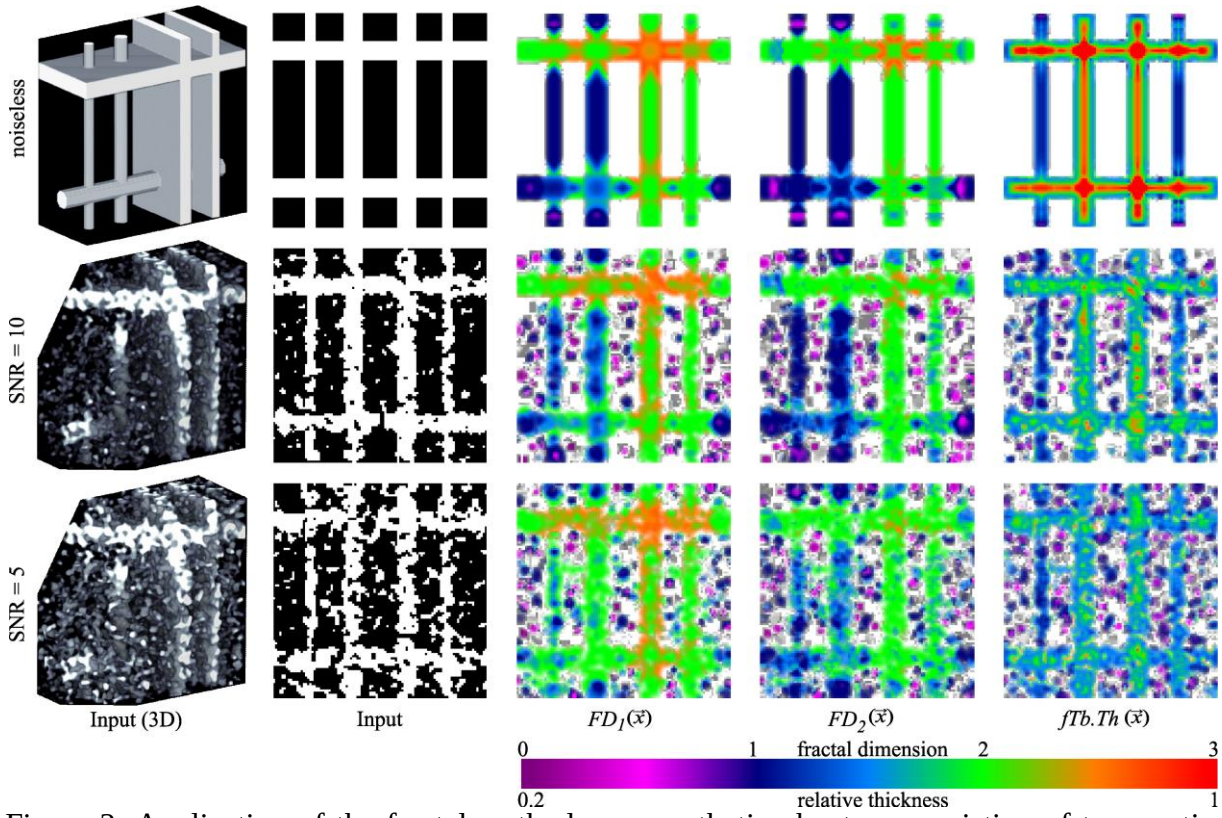

Figure 2: Application of the fractal method on a synthetic phantom consisting of two vertical rods and plates and one horizontal rod and plate of different thickness. Rows: 1) noiseless phantom, 2) signal-to-noise ratio=10, 3) signal-to-noise ratio=5. Columns: 1) volumetric rendering, 2) middle slice through the phantom, 3) $FD_1(\vec{x})$, 4) $FD_2(\vec{x})$, 5) $\mathrm{fTb.Th}(\vec{x})$.

Vertebral specimens and image data

Two data sets were analyzed: one to obtain robustness of the method with respect to precision and accuracy, the other to predict failure load F_{exp} and to obtain correlations between all parameters. For the first experiment, five human T_{12} vertebral specimens were harvested from deceased donors, surrounding soft tissue and marrow was removed and the vertebrae were then embedded in epoxy resin. The vertebra phantoms were repeatedly scanned on a clinical CT scanner under simulated in vivo conditions, see Fig. 3. Two protocols, a high-resolution (355mAs) and a standard resolution (140mAs) were applied, both with 120kVp and voxel size 188×188×300µm³. Three repetitions were performed with image noise as found under *in vivo*

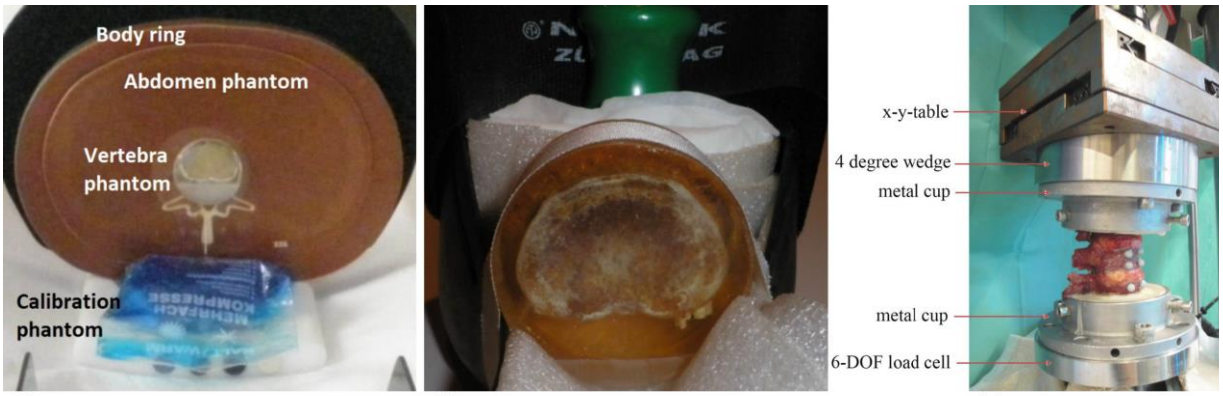

Figure 3: (a) setup for the simulated in-vivo QCT scan of the vertebra phantom containing the abdomen and calibration phantom (b) HRpQCT inset for ground-truth scan (c) setup to measure the failure load F_{exp} from the BioAsset specimen.

conditions (abdomen phantom) and two with increased image noise (abdomen phantom with additional body ring). For reference purposes, HRpQCT scans of the vertebra phantoms were obtained (XtremeCT I, Osteoporose Praxis Neuer Wall, Hamburg, Germany, standard patient protocol), details of which were published elsewhere[19,20]. All scans were calibrated from Hounsfield (HU) to mineral scale (mg/cm³), and a cylindrical volume-of-interest (VOI) was placed within the trabecular region of all vertebrae, sub-divided into four segments (volume≈1.1-1.7cm³, $1.02 \cdot 10^5$-$1.64 \cdot 10^5$voxels) and automatically registered between all repeated scans (Fig. 4).

The second experiment was derived out of a larger *ex situ* study (BioAsset[21]) performed in total on 33 deceased patients who had osteoporosis. Each spinal specimen contained three vertebrae (T_{11}, T_{12}, L_1) and their respective intermediate intervertebral discs. The vertebrae were scanned and calibrated with the same HRQCT procedure as used for the vertebrae phantoms, but segmented with one Pacman-shaped VOI per vertebra. HRQCT data of 76 vertebrae remained after excluding not sufficiently large VOIs. Data of the maximum failure load F_{exp} at T_{12} was experimentally derived from a subset of 20 patients[22]. The spinal segments were fixed to a servo-hydraulic testing machine (Bionix 858.2, MTS Systems, Eden Prairie, MN, USA). After

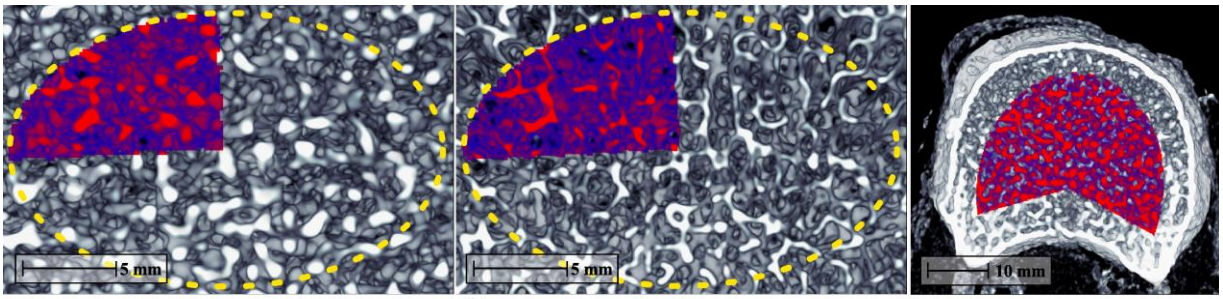

Figure 4: Transversal ray-tracing projection of the vertebral CT-scans. (a) Embedded vertebra subvolume from HRQCT scan and representative cylindrical VOI with one of four sub-VOIs, (b) corresponding HRpQCT scan, (c) HRQCT BioAsset scan with one Pacman-shaped VOI per vertebra.

preconditioning, a quasistatic uniaxial compression (6 mm/min) with a 4-degree flexion angle was applied on each spinal segment until resulting failure of the middle vertebral body (T_{12}). Further details of the loading can be found elsewhere[23]. 17 T_{12} vertebrae remained for correlations between F_{exp} and HRQCT parameters after excluding those with an insufficient size.

The following standard parameters were computed: bone mineral density (BMD), bone volume fraction (BV/TV) and tissue mineral density (TMD); with a model dependent method trabecular number (Tb.N), mean intercept length (MIL) and bone surface ratio (BS/BV); and model independently[24] trabecular separation (Tb.Sp), trabecular thickness (Tb.Th) and structure model index (SMI, http://bruker-microct.com/next/CTAn03.pdf). The threshold for computing the micro-structural and fractal parameters was group-wise adjusted to compensate systematic differences between the QCT, HRQCT and HRpQCT scans. A histogram-based correction from a Gaussian fit of the mean BMD and standard deviation of each setting was applied[25,26]. The threshold was selected in order to obtain $BV/TV \approx 10\%$ on HRpQCT[27] and $BV/TV \approx 25\%$ on QCT and HRQCT. Calibration of the HRpQCT scans was performed with the scanner's software (Scanco Medical AG, Brüttisellen, Switzerland) and registration, calibration, and computation of

the standard parameters were performed with Structural *Insight* (v3.1, Biomedical Imaging, University of Kiel, Germany).

Statistical analysis

Precision and accuracy were derived from the vertebra phantoms. The normalized short-term precision for repeated scans (STP) was used as a metric of precision and reproducibility:

$$STP = \sqrt{\frac{\sum_{i=1}^{N}\sum_{j=1}^{M}(x_{ij}-\bar{x}_i)^2}{N(M-1)(\max_i\{\tilde{x}_i\}-\min_i\{\tilde{x}_i\})^2}}, \quad (13)$$

with $N = 20$ the number of VOIs, $M = 10$ the number of repeated scans per VOI, x_{ij} the structural parameter at VOI i and scan j, $\bar{x}_i$ its arithmetic mean and $\tilde{x}_i$ the median at VOI i. The normalized long-term precision (LTP) was used as a metric of accuracy or trueness. It relates the median QCT structural parameter $\tilde{x}_i$ at VOI i with the ground-truth HRpQCT parameter y_i:

$$LTP = \sqrt{\frac{\sum_{i=1}^{N}(y_i-\hat{y}_i)^2}{(N-2)(\max_i\{y_i\}-\min_i\{y_i\})^2}}, \quad (14)$$

with $\hat{y}_i = a + b\,\tilde{x}_i$ the linear estimate of y_i from the QCT. The sample size and the number of repeated scans were sufficient to claim statistical significance at a level considered sufficient for characterizing STP and LTP [28].

Average, standard deviation, quartiles, and Spearman's rank correlation coefficients (ρ) were computed from the BioAsset data (76 vertebrae), *p*-values were Bonferroni-corrected for multiple comparisons. For 17 vertebrae, linear models for the prediction of F_{Exp} were derived from BMD in combination with up to three micro-structural parameters. R^2, RMSE, and adjusted R^2 (adjR^2) were computed and a robust R^2 (robR^2) and RMSE (robRMSE) were obtained from leave-one-out cross-validation of all combinations. The optimum regression models between F_{exp} and fractal or standard structural parameters were selected as those with the minimum corrected Akaike information criterion (AICc).The AICc is superior to the Bayes Information criterion[29]

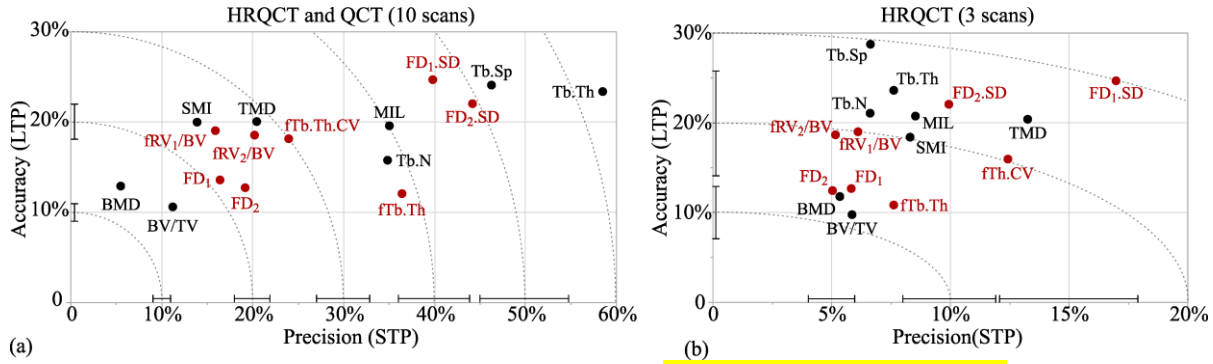

Figure 5: Precision (STP) vs. accuracy (LTP) with confidence intervals. Lowest values represent highest trueness and reproducibility, isobars depict compound errors of both metrics, (a) ten scans (HRQCT and QCT with and without body ring, confidence intervals of $p<0.025$), (b) three scans (HRQCT without additional body ring, confidence intervals of $p<0.1$).

and more widely applied for those analyses[30]. The gain of information between two models can be assessed by the relative likelihood: $p(m_1\ vs\ m_2) = \exp\left(\frac{AICc(m_1)-AICc(m_2)}{2}\right)$ with m_1 and m_2 the models. The analysis was performed with JMP (v11, SAS Institute Inc., Cary, NC, USA) and MATLAB.

Results

Precision and Accuracy

Figure 5a shows the precision (STP) and accuracy (LTP) of all structural parameters on ten repeated scans. Highest precision and accuracy (STP, LTP) were obtained by BMD (6%, 13%) and BV/TV (11%, 11%). From the micro-structural parameters, FD (16-19%, 13%) was most robust, followed by fRV/BV (16-20%, 19%), SMI (14%, 20%), and TMD (20%, 20%). The parameter fTb.Th contained low precision but high accuracy (36%, 12%). However, its pendant Tb.Th (58%, 32%) still contained higher errors regarding both metrics. If considering only three repeated scans with a minimum noise level (Fig. 5b), STP generally decreased while LTP remained unchanged. In particular, FD (5-6%, 12-13%), fRV/BV (5-6%, 19%) and fTb.Th

Parameter	Avg	SD	Q_1	Q_3
FD_1	2.12	.04	2.08	2.15
FD_2	1.57	.05	1.54	1.60
FD_1.SD	.32	.02	.30	.34
FD_2.SD	.32	.03	.30	.34
fRV_1/BV[%]	29.3	6.6	24.0	35.0
fRV_2/BV[%]	28.6	6.1	23.7	32.7
fTb.Th[*mm*]	1.10	.02	1.09	1.12
fTb.Th.CV[%]	13.8	.5	12.3	13.3
BMD[mg/cm^3]	54.0	19.5	43.8	69.2
TMD[mg/cm^3]	206.1	7.8	201.7	211.8
BV/TV[%]	25.0	1.5	24.0	26.1
Tb.N[mm^{-1}]	.67	.07	.62	.72
Tb.Th[*mm*]	.39	.05	.35	.43
Tb.Sp[*mm*]	.95	.13	.85	1.04
SMI	.16	.10	.08	.22
F_{exp}[*kN*]	2.10	.50	1.75	2.47
Age[*y*]	80.9	7.1	75.5	86.0
BMI[kg/m^2]	22.4	4.7	18.7	26.5

Table 1: Fractal, densitometric and micro-structural parameters (N=76), F_{exp} (N=20) and donor's characteristics (N=33).

(8%,11%) obtained similar robustness as BMD (5%, 12%) and BV/TV (6%, 10%). Improved precision was also observed on FD_2.SD, Tb.N, Tb.Th and Tb.Sp.

Descriptive statistics and correlations between parameters

The parameter FD_1 showed higher values than FD_2, while values of fRV_1/BV and FD_1.SD were similar to fRV_2/BV and FD_2.SD, respectively (Tab. 1). The parameter fTb.Th contained higher estimates than Tb.Th (and Tb.Sp) but reduced variation (SD/Avg). Spearman's rank correlation coefficients (ρ) between all parameters are shown in Tab. 2 with the exception of BS/BV, since it contained the same values as MIL. In general, the standard parameters correlated with each other, as did the fractal parameters, while the correlation between parameters of both groups was rather low. An exceptions was fTb.Th which contained significant correlations to all parameters with exception of BMD and FD.SD. The correlation between fTb.Th and Tb.Th (ρ=0.75*) was not noticeably stronger than between fTb.Th and other structural parameters (Tb.N: ρ=-0.79*, SMI: ρ=0.84*).

	BMD	FD_1	FD_1.SD	fRV_1/BV	FD_2	FD_2.SD	fRV_2/BV	fTb.Th	fTb.Th.CV	BV/TV	TMD	Tb.N	Tb.Th	Tb.Sp	MIL	SMI
FD_1	.00															
FD_1.SD	.29	.28														
fRV_1/BV	.05	**-.98***	-.12													
FD_2	.06	**.96***	**.43***	**-.91***												
FD_2.SD	.21	**.47***	**.94***	-.32	**.63***											
fRV_2/BV	.00	**-.98***	-.25	**.97***	**-.98***	**-.46***										
fTb.Th	-.11	**-.79***	-.27	**.77***	**-.67***	-.33	**.68***									
fTb.Th.CV	.13	**.74***	**.55***	**-.67***	**.72***	**.60***	**-.66***	**-.87***								
BV/TV	.38	.15	-.03	-.18	.03	-.11	-.06	**-.59***	.35							
TMD	-.01	-.31	-.05	.30	-.16	-.01	.17	**.65***	-.40*	**-.61***						
Tb.N	-.04	.37	-.12	-.40*	.16	-.14	-.22	**-.79***	**.50***	**.73***	**-.72***					
Tb.Th	.15	-.36	.11	.39	-.15	.13	.20	**.75***	**-.49***	**-.55***	**.73***	**-.96***				
Tb.Sp	.05	-.34	.10	.37	-.13	.14	.19	**.75***	**-.47***	**-.66***	**.66***	**-.98***	**.95***			
MIL	.32	-.39	.16	.41*	-.17	.14	.24	**.66***	-.43*	-.27	**.58***	**-.84***	**.93***	**.86***		
SMI	-.05	**-.48***	.07	**.51***	-.29	.05	.35	**.84***	**-.55***	**-.77***	**.75***	**-.94***	**.87***	**.87***	**.72***	
F_{exp}	**.84***	-.14	.71	.30	.04	.45	.05	-.05	.32	.25	-.05	-.20	.24	.20	.47	.11

Table 2: Spearman's rank correlation coefficients (ρ) between density, fractal dimension, micro-architectural parameters (N=76) and vertebral failure load (N=17), *p<0.05, bold p<0.01 (two-tailed correlation is significant with Bonferroni correction).

Multiple regression analysis with failure load as dependent variable

Table 3 and Fig. 6 show multiple linear regression models to explain the variability of F_{exp}. The first set (S_1 to S_4) was based on BMD and (non-fractal) standard parameters, the second set (F_1 to F_4) was based on BMD and fractal parameters. The indices of the model names indicate the number of used predictors. Although the actual predictors were chosen independently as the combination that minimizes the AICc, the best models contained always all predictors of the best preceding models (for instance $S_4 = S_3$ + TMD).

	S_1 or F_1	*S_2*	*S_3*	*S_4*		*F_2*	*F_3*	*F_4*
BMD	<.0001*	.0002*	.0002*	.0007*	BMD	<.0001*	<.0001*	<.0001*
MIL	-	.188	.043*	.095	FD_1.SD	.015*	.0008*	.0005*
BS/BV	-	-	.053	.151	FD_2	-	.011*	.018*
TMD	-	-	-	.213	fRV_2/BV	-	-	.036*
AICc	2.813	4.123	3.172	5.830	AICc	-1.139	-5.900	-7.478

Table 3: p-values of the predictors (*p<0.05) and total AICc obtained from optimal models for prediction of F_{exp} with and without incorporating fractal methods.

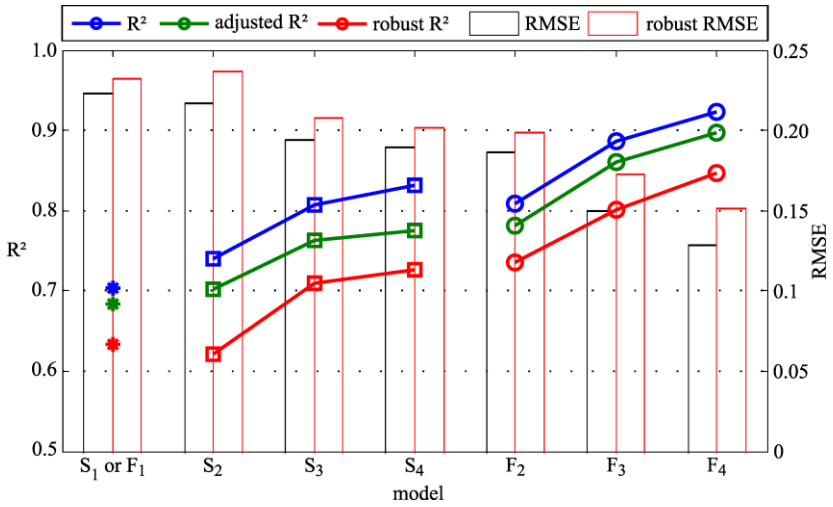

Figure 6: R^2, $adjR^2$, $robR^2$, RMSE and robRMSE of linear models for prediction of Fexp.

The highest simple correlation with F_{Exp} was obtained by BMD (S_1=F_1: $adjR^2$=0.684, $robR^2$=0.634, robRMSE=0.231, AICc=2.81). The AICc's indicated a significant gain of information by $F_{2\text{-}4}$ compared to $S_{1\text{-}4}$. Model F_2 with BMD and FD_1.SD ($adjR^2$=0.782, $robR^2$=0.736, robRMSE=0.197, AICc=-1.14) obtained already higher correlations and lower errors than all S-models. Adding additionally FD_2 as a predictor (model F_3: $adjR^2$=0.861, $robR^2$=0.801, robRMSE=0.171, AICc=-5.90) significantly raised the gain of information towards standard models ($p(F_3$ *vs* $S_{1\text{-}4})$=0.003* to 0.013*). The optimum model was obtained by adding fRV_2/BV as a further predictor (model F_4: $adjR^2$=0.897, $robR^2$=0.847, robRMSE=0.150, AICc=-7.48), yielding a significant gain of information towards $S_{1\text{-}4}$ ($p(F_4$ *vs* $S_{1\text{-}4})$=0.001* to 0.006*) and F_2 ($p(F_4$ *vs* $F_2)$=0.042*). P-values of the parameter estimates (Tab. 3) showed significant contributions of all fractal parameters to the F-models while standard parameters, with exception of MIL in model S_3, did not contribute significantly to the S-models. When allowing only parameters obtained with the first fractal method, the predictors FD_2 and fRV_2/BV of model F_3 and F_4 have been replaced by FD_1 and fRV_1/BV. These models with three ($adjR^2$=0.844, $robR^2$=0.771, robRMSE=0.186, AICc=-3.97) and four predictors ($adjR^2$=0.891, $robR^2$=0.833,

robRMSE=0.157, AICc=-6.48) were not significant different to the models F_3 and F_4 based on both fractal methods. Models, based on the Bayes information criterion were identical to these selected with the AICc.

Discussion

Compared to standard micro-structural parameters, the fractal methodology improved the prediction of failure load and showed robustness against image noise. In particular FD.SD, FD and fRV/BV demonstrated to be well-adjusted for the analysis of HRQCT volumes. Prediction of failure load with standard micro-structure parameters can explain up to 86% of the variability in vertebral failure load, for instance by using a linear model of BMD, SMI and DA on HRpQCT (isotropic resolution 82µm)[31]. However, such predictive power has not been observed before on HRQCT due to the high sensitivity of noise of standard micro-structural parameters.

Regression models with standard structural parameters ($S_{2\text{-}4}$) were not able to extract additional information of F_{exp}. Conversely, the fractal model F_3, based on BMD, FD_1.SD and FD_2, explained 86% (adjR^2) of vertebral failure load on *in vivo*-like image conditions, thus bridging the gap between *ex vivo* and *in vivo*. Model F_4, based on BMD, FD_1.SD, FD_2 and fRV_2/BV, explained up to 90% (adjR^2) of the variability of F_{exp}. Models F_3 and F_4 significantly improved the extraction of information beyond BMD without over-fitting, as indicated by AICc's, robR^2 and robRMSE. This highlights the different aspects of bone quality captured by the set of fractal parameters. Our results also showed that the same fractal parameters obtained with the either of the both fractal methods were nearly redundant as they did not add independent information in any linear regression model and also showed high Spearman's rank correlations (FD: ρ=0.96*, FD.SD: ρ=0.94*, fRV/BV: ρ=0.97*). Thus, for the prediction of failure load, one

could simply implement the first fractal method rather than both methods, explaining 84% (adjR^2) with the model of three and 89% with the model of four predictors.

Robustness against image degradation is particularly important for *in vivo* micro-structural parameters. Precision or reproducibility (STP) is important to derive longitudinal skeletal changes. Accuracy or trueness (LTP), on the other hand, reflects robustness against inhomogeneous settings (different protocols, scanners) and defines, in particular, the ability to translate results of phantom- to patient studies[28]. In this study, both the accuracy and precision of the structural information improved if computed with fractal methods. In particular, fTb.Th improved the accuracy of Tb.Th though still significantly correlated (ρ(fTb.Th,Tb.Th) =0.75*).

The parameters fRV/BV and FD improved the accuracy of SMI. However, in contrast to fRV/BV and FD, SMI generally measures the convexity of the trabecular bone rather than its structural model[32]. This might explain the weak correlations between SMI and the related fractal parameters (FD_1: ρ=-0.48*, fRV_1/BV: ρ=0.51*, FD_2: ρ=-0.29, fRV_2/BV ρ=0.35). Results of fRV/BV (mean: 29%, SD: 6.4%) showed agreement with an alternative parameter of RV/BV on HRpQCT resolution[27] (mean: 17.5%, SD: 6.9%). This indicates the inadequacy of the strict parallel plate model in the vertebral domain.

High correlations with F_{exp} were only obtained with BMD (ρ=0.84*) and FD.SD (ρ=0.71). The BMD was not correlated with the fractal parameters FD (ρ=0.0 – 0.06), FD.SD (ρ=0.21 – 0.29) and fRV/BV (ρ=0.0 – 0.05), while BMD and all of these fractal parameters contributed significantly to the prediction of F_{exp} in model $F_{2\text{-}4}$. Hence the fractal parameters are able to characterize failure load from the bone micro-structure rather than from the bone density, as obtained with BMD.

In general, unless one defines a mathematical mapping between hidden fine scale structural information and visible coarse scale information, high noise and low effective *in vivo*

resolution (500×500×650µm³)[5] impedes ability to obtain failure load from bone in *in vivo* HRQCT volumes. Self-similarity, the property to extrapolate structural information from coarse to fine scale, makes fractal methods robust against low resolution and image degradation due to noise. Scale invariance and thus, accuracy, applies almost completely to fractal methods, but not to standard micro-structural parameters.

Most algorithms of micro-structural parameters require a crisp threshold which discards a great portion of the contained information. In contrast, the fractal methods proposed here not only allow the application of a crisp threshold, but also application of a sigmoidal fuzzy threshold. Nevertheless, the conducted experiments required the choice of a crisp threshold for the purpose of a fair comparison between fractal and standard parameters. The threshold was individually adapted from the histogram to remove most correlations of the micro-structural parameters with BMD[25]. Alternative tests with global thresholds of 150, 200 and 250mg/cm³ showed less performance on the standard micro-structural parameters, which means higher correlation with BMD and lower ability to predict failure load.

Finally, some alternative uses can be drawn from the method proposed here. Local qualitative indicators of bone health $FD_1(\vec{x})$, $FD_2(\vec{x})$ and $fTb.Th(\vec{x})$ (Fig. 2) could be beneficial for the segmentation of multiple myeloma[33], or to extend the local information of finite element models[23,34]. Furthermore, replacing the input volume with a skeletonized version of the bone[5] likely improves the estimation of $FD_1(\vec{x})$ and $FD_2(\vec{x})$ but however, impairs the estimation of $fTb.Th(\vec{x})$. Conversely, since skeletonization is a complex task in 3D, as noise and uncertainties need to be carefully treated without removing the relevant plates and rods, this adjustment might be only reasonable on HRpQCT.

Conclusion

The new fractal method proposed for the analysis of clinical 3D QCT and HRQCT volumes computes the RV/BV and Tb.Th. It does not require a well-defined skeleton, and is applicable with fuzzy threshold functions. Precision and accuracy tests demonstrated that the method can withstand image noise from *in vivo* conditions. The fractal measurements outperformed most of the micro-structural parameters in precision (STP) by as much as 20-45% (MIL, Tb.Sp, Tb.Th). The accuracy (LTP) of fractal parameters FD and fTb.Th was almost as high as that of BMD or BV/TV. On the *ex vivo* human vertebrae, HRQCT-based linear prediction models of failure load improved significantly by using fractal rather than standard predictors, and can exceed the quality of reported predictive models of *ex vivo* HRpQCT resolution[31]. Thus, application of fractal methods may grant further insight in the study of bone quality *in vivo* when image resolution and quality are less than optimal for current standard methods.

Acknowledgments

This work was supported by the German Federal Ministry of Education and Research (BMBF) under Grant 01EC1005C, by a doctoral fellowship funding from Argentinean National Scientific and Technical Research Council (CONICET) and by the Chinese Fundamental Research Funds for the Central Universities under Grant DUT15RC(3)130. The authors acknowledge Isolde Frieling and Beata Hoffmann for obtaining the volumes, Jan Bastgen for building the vertebra phantoms, Samuel G. Hoare, and the reviewers and editors for their helpful comments.

Disclosure of conflicts of interest

The authors have no relevant conflicts of interest to disclose.

Appendix A: Implementation of the local fractal dimension

To compute the fractal measures on digital volumes of spongy bone, the mass $M_r(\vec{x})$ at voxel $\vec{x}$ was derived with a convolution of a bone map $Bone(\vec{x})$ and a structural element $SE_r \in [0,1]$: $M_r(\vec{x}) = (Bone \circ SE_r)(\vec{x})$. For every voxel, the masses of 25 different radii were computed $r_i = 0.3\,(\frac{1.0}{0.3})^{(i-1)/24}, i \in \{1,\dots,25\}$ thus generating a constant $a = r_{i+1}/r_i = r_2/0.3$, as used in equation (1) and (3). The generalized conversion from an calibrated CT volume $I(\vec{x})$ to $Bone(\vec{x})$ uses the sigmoidal cumulative normal distribution:

$$Bone_{t,\sigma}(\vec{x}) = \Phi_{t,\sigma}\big(\mathrm{I}(\vec{x})\big) = \int_{-\infty}^{I(\vec{x})} \frac{1}{\sqrt{2\sigma^2\pi}} \exp\left(\frac{(v-t)^2}{-2\sigma^2}\right) dv, \quad (15)$$

where t is the threshold and $\sigma \geq 0$ a fuzziness parameter; $Bone_{t,0}(\vec{x})$ is the binary non-fuzzy bone map. The continuous structural element SE_r [35], which allows to vary the radius r independently of the voxel size $\vec{\epsilon}$, reads:

$$SE_r(\vec{c}) = \iiint_{-\vec{\epsilon}}^{\vec{\epsilon}} \frac{H(r-\|\vec{c}+\vec{\vartheta}\|)}{8\epsilon_x\epsilon_y\epsilon_z}\, d\vartheta_x\, d\vartheta_y\, d\vartheta_z, \quad (16)$$

with $\vec{c}$ the position inside the structural element, $\|\cdot\|$ the Euclidean norm and $H(\cdot)$ the Heaviside function. The ridge map $Ridge(\vec{x})$ was obtained from the bone map $Bone(\vec{x})$:

$$Ridge(\vec{x}) = \frac{(Bone \circ SE_k)^{\mathrm{q}}(\vec{x})}{\sum_{\vec{c}} SE_k(\vec{c})}, \quad (17)$$

with k the a-priori approximation of the trabecular thickness and q≈3 (>1) a parameter to steer the sharpness of the thinning procedure. Accurate local estimates of $FD_i(\vec{x})$ and $fTb.Th(\vec{x})$ were obtained only on the central ridge of the structure. The correction for voxels, which did not belong to the bone ridge were computed with a voxel-wise smoothing operator:

$$\overline{S(\vec{x})} = \frac{((S \cdot Ridge) * SE_k)(\vec{x})}{(Ridge * SE_k)(\vec{x})}, \quad (18)$$

where $S(\vec{x})$ is a placeholder of $FD_i(\vec{x})$ or $fTb.Th(\vec{x})$, and $*$ the 3D convolution operator. The fractal plate volume ratio is given by $\mathrm{fPV/BV} = 1 - \mathrm{RV/BV}$.

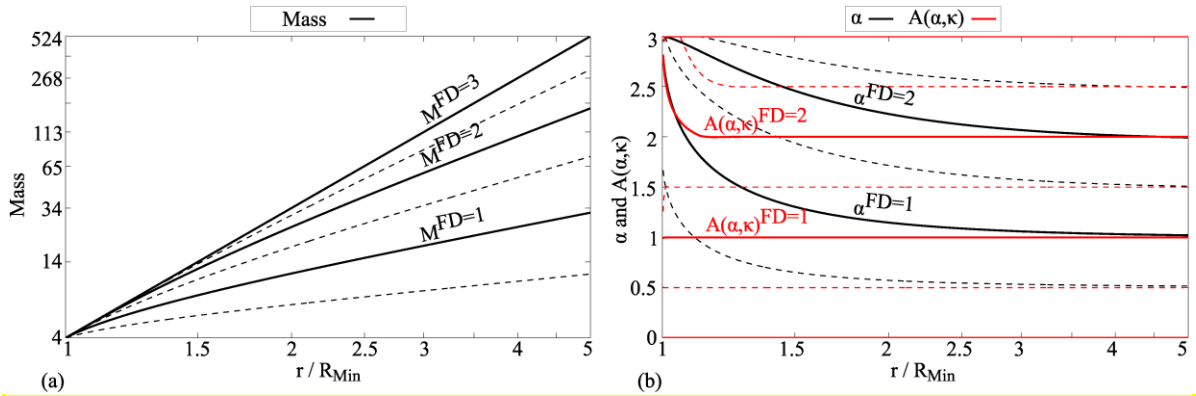

Figure 7: (a) Evolution of the prototype masses with r for FD =0,0.5, 1, ... 3, (b) Hölder exponents α and $A(\alpha,\kappa)$ of the prototype and interpolated volumes.

The functions $A(\alpha,\kappa)$ and $\Omega(\alpha, FD/\alpha)$ were derived from the evolution of the intersection of a sphere of radius r with a sphere, rod, plate of radius R_{Min}, representing the integer fractal dimensions 0, 1 and 2. The fractal dimension 3 was directly obtained from the volume of a sphere with radius r. The masses of these structures are:

$$M_r^{FD} = \begin{cases} 4/3\pi R_{Min}^3, & if\ (FD = 0 \wedge r > R_{Min}) \\ 4\pi R_{Min}^2 \hat{r} + \pi/3(r-\hat{r})^3 + \pi R_{Min}^2 (r-\hat{r}), & if\ (FD = 1 \wedge r > R_{Min}) \\ \pi R_{Min}/3(6\,r^2 - 2R_{Min}^2), & if\ (FD = 2 \wedge r > R_{Min}) \\ 4/3\pi r^3, & if\ (FD = 3 \vee r \leq R_{Min}) \end{cases}, \quad (19)$$

with $\hat{r} = (r^2 - R_{Min}^2)^{1/2}$. The logarithms of these volumes were then interpolated for non integer fractal dimensions and the slope α and the curvature κ, expressed in radians, were computed for $r \in [0, 10\,R_{Min}]$. To obtain the map $A(\alpha,\kappa)$, the known fractal dimension FD was fitted as a surface of α and κ. Figure 7 shows the evolution of the volumes and the estimates of α and $A(\alpha,\kappa)$, α requires much larger radii ($r > 3\,R_{Min}$) to obtain a close estimate to the true fractal dimension than $A(\alpha,\kappa)$ ($r > 1.2\,R_{Min}$). In a similar way to the estimation of the fractal dimension, the map for the trabecular thickness $\Omega(\alpha, FD/\alpha)$was obtained from the known values of r/R_{Min} as a surface interpolation of α and FD/α.

References

[1] D.W. Dempster, "The impact of bone turnover and bone-active agents on bone quality: focus on the hip" Osteoporosis Int **13**(5), pp. 349-352 (2002).

[2] M.A. Haidekker and G. Dougherty, "Medical imaging in the diagnosis of osteoporosis and estimation of the individual bone fracture risk," in Medical Image Processing, edited by G. Dougherty (Springer, New York, Dordrecht, Heidelberg, London, 2011), pp. 193-225.

[3] S. Svensson, "Centres of maximal balls extracted from a fuzzy distance transform," Proceedings of the 8th International Symposium on Mathematical Morphology, 19-20 (2007).

[4] A. Darabi, F. Chandelier, and G. Baroud, "Thickness analysis and reconstruction of trabecular bone and bone substitute microstructure based on fuzzy distance map using both ridge and thinning skeletonization," Can J Elect Comput E **34**(1/2), 57-62 (2009).

[5] A. Krebs, C. Graeff, I. Frieling, B. Kurz, W. Timm,K. Engelke, and C.-C. Glüer, "High resolution computed tomography of the vertebrae yields accurate information on trabecular distances if processed by 3D fuzzy segmentation approaches," Bone **44**(1), 145-152 (2009).

[6] P. K. Saha, Y. Xu, H. Duan, A. Heiner, and G. Liang, "Volumetric topological analysis: a novel approach for trabecular bone classification on the continuum between plates and rods," IEEE T Med Imaging **29**(11), 1821-1838 (2010).

[7] R. Moreno, Ö. Smedby, and M. Borga, "Soft classification of trabeculae in trabecular bone," I S Biomed Imaging, 1641-1644 (2011).

[8] R. Moreno, M. Borga, and Ö. Smedby, "Evaluation of the plate-rod model assumption of trabecular bone," I S Biomed Imaging, 470-473 (2012).

[9] B. Vasilić, C.S. Rajapakse, and F. W. Wehrli, "Classification of trabeculae into three-dimensional rodlike and platelike structures via local inertial anisotropy," Med Phys **36**(7), 3280-3291 (2009).

[10] P.K. Saha, B. R. Gomberg, and F. W. Wehrli, "Three-dimensional digital topological characterization of cancellous bone architecture," Int J Imag Syst Tech **11**(1), 81-90 (2000).

[11] C. S. Fortin, R. Kumaresan, W. J. Ohley, and S. Hoefer, "Fractal dimension in the analysis of medical images," IEEE Eng Med Biol, **11**(2), 65-71 (1992).

[12] A. F. Silvetti and C. A. Delrieux, "Quadratic self-correlation: An improved method for computing local fractal dimension in remote sensing imagery," Comput Geosci **60**, 142-155 (2013).

[13] L. Pothuaud, P. Carceller, and D. Hans, "Correlations between grey-level variations in 2D projection images (TBS) and 3D microarchitecture: applications in the study of human trabecular bone microarchitecture," Bone **42**(4), 775-787 (2008).

[14] B. C. Silva, W. D. Leslie, H. Resch, O. Lamy, O. Lesnyak, N. Binkley, E. V. McCloskey, J.A. Kanis, and J. P. Bilezikian, "Trabecular bone score: a noninvasive analytical method based upon the DXA image," J Bone Miner Res **29**(3), 518-530 (2014).

[15] G. Maquer, Y. Lu, E. Dall'Ara, Y. Chevalier, M Krause, L. Yang, R. Eastell, K. Lippuner, and P. K. Zysset, "The Initial Slope of the Variogram, Foundation of the Trabecular Bone Score, Is Not or Is Poorly Associated With Vertebral Strength," J Bone Miner Res **31**(2), 341-346 (2015).

[16] S. Novianto, Y. Suzuki, and J. Maeda, "Near optimum estimation of local fractal dimension for image segmentation," Pattern Recogn Lett **24**, 365-374 (2003).

[17] R. Lopes and N. Betrouni, "Fractal and multifractal analysis: A review," Med Image Anal **13**(4), 634-649 (2009).

[18] L. Rimoldini, "Weighted skewness and kurtosis unbiased by sample size and Gaussian uncertainties," Astronomy and Computing **5**, 1-8 (2014).

[19] F. Thomsen, J. Peña, J. Bastgen, B. Hoffmann, I. Frieling, C.-C. Glüer, and C. Delrieux, "Binary Local Fractal Dimension: a Precise Structure Parameter for 3D High Resolution Computed Tomography Images of the Human Spongiosa," Argentine Symposium on Technology **14**, 232-243 (2013).

[20] J. Peña, F. Thomsen, T. Damm, G. Campbell, J. Bastgen, R. Barkmann, and C.-C. Glüer, "Bone-Marrow Densitometry: Assessment of Marrow Space of Human Vertebrae by Single Energy High Resolution Quantitative Computed Tomography," Med Phys **43**(7), 4174-4183 (2016).

[21] C.-C. Glüer, M. Krause, O. Museyko, B. Wulff, G. Campbell, T. Damm, M. Daugschies, G. Huber, Y. Lu, J. Peña, S. Waldhausen, J. Bastgen, K. Rohde, I. Steinebach, F. Thomsen, M. Amling, R. Barkmann, K. Engelke, M. Morlock, J. Pfeilschifter, and K. Püschel, "New horizons for the in vivo assessment of major aspects of bone quality Microstructure and material properties assessed by Quantitative Computed Tomography and Quantitative Ultrasound methods developed by the BioAsset consortium," Osteologie **22**(3), 223-233 (2013).

[22] Y. Lu, M. Krause, N. Bishop, K. Sellenschloh, C.-C. Glüer, K. Püschel, M. Amling, M. Morlock, and G. Huber, "The role of patient-mode high-resolution peripheral quantitative computed tomography indices in the prediction of failure strength of the elderly women's thoracic vertebral body," Osteoporosis Int **26**(1), 237-244 (2015).

[23] Y. Lu, G. Maquer, O. Museyko, K. Püschel, K. Engelke, P. Zysset, M. Morlock, and G. Huber, "Finite element analyses of human vertebral bodies embedded in polymethylmethalcrylate or loaded via the hyperelastic intervertebral disc models provide equivalent predictions of experimental strength," J Biomech **47**(10), 2512-2516 (2014).

[24] T. Hildebrand and P. Rüegsegger, "A new method for the model-independent assessment of thickness in three-dimensional images," Journal of Microscopy **185**(1), 67-75 (1997).

[25] M. A. Haidekker, R. Andresen, C. Evertsz, D. Banzer, and H. Peitgen, "Issues of threshold selection when determining the fractal dimension in HRCT slices of lumbar vertebrae," Brit J Radiol **73**(865), 69-72 (2000).

[26] A. I. Hussein and E. F. Morgan, "The effect of intravertebral heterogeneity in microstructure on vertebral strength and failure patterns," Osteoporosis Int **24**(3), 979-989 (2013).

[27] X. S. Liu, P. Sajda, P. K. Saha, F. W. Wehrli, G. Bevill, T. Keaveny, and X. Guo, "Complete volumetric decomposition of individual trabecular plates and rods and its morphological correlations with anisotropic elastic moduli in human trabecular bone," J Bone Miner Res **23**(2), 223-235 (2008).

[28] C.-C. Glüer, G. M. Blake, Y. Lu, B. A. Blunt, M. Jergas, H. K. Genant, "Accurate assessment of precision errors: How to measure the reproducibility of bone densitometry techniques," Osteoporosis Int **5**(4), 262-270 (1995).

[29] K. P. Burnham and D. R. Anderson, "Multimodal inference understanding AIC and BIC in model selection," Sociological methods & research **33**(2), 261-304 (2004).

[30] A. Ken, D Derryberry, and T. Peterson, "Model selection for ecologists: the worldviews of AIC and BIC." Ecology 95 (3), 631-636 (2014)

[31] J. Wegrzyn, J.-P. Roux, M. E. Arlot, S. Boutroy, N. Vilayphiou, O. Guyen, P. D. Delmas, R. Chapurlat, and M. L. Bouxsein, "Role of trabecular microarchitecture and its heterogeneity parameters in the mechanical behavior of ex vivo human L3 vertebrae," J Bone Miner Res **25**(11), 2324-2331 (2010).

[32] P. L. Salmon, C. Ohlsson, S. J. Shefelbine, M. Doube, "Structure model index does not measure rods and plates in trabecular bone," Front Endocrinol **6** (2015).

[33] J. Borggrefe, S. Giravent, F. Thomsen, J. Peña, G. Campbell, A. Wulff, A. Günther, M. Heller, and C.-C. Glüer, "Association of QCT Bone Mineral Density and Bone Structure With Vertebral Fractures in Patients With Multiple Myeloma," J Bone Miner Res **30**(7), 1329-1337 (2015).

[34] G. Campbell, J. Peña, S. Giravent, F. Thomsen, T. Damm, C.-C. Glüer, "Assessment of Bone Fragility in Patients with Multiple Myeloma Using QCT- Based Finite Element Modelling," J Bone Miner Res (2016).

[35] R. Moreno, M. Borga, and Ö. Smedby, "Estimation of trabecular thickness in gray-scale images through granulometric analysis," Proceedings of SPIE, 831451 (2012).